CCS Chemistry

RESEARCH ARTICLE

Received: Feb. 9, 2025 | Accepted: May 2, 2025 | Published: June 14, 2025

Identification of Cu-N_2 Sites for Zn-Air Batteries in Harsh Electrolytes: Computer Virtual Screening, Machine Learning, and Practical Application

Chenxi Xu[1,2†], Kaiqi Li[3†], Shengchao Liu[4†], Junwei Xu[1], Subash Sharma[5], Jincan Zhang[5], Boyang Mao[5], Haotian Chen[6], Hao Zhang[6*], Hannan Xu[7], Bingcheng Luo[8*], Haiteng Zhao[9], Zhuoxinran Li[10], Zhongyuan Huang[1*], Jianan Wang[11], Kai Xi[11], Chaopeng Fu[12], Yunlong Zhao[13], Guoliang Chai[14], Guanjie He[3*], Ivan Parkin[3*] & Huanxin Li[3,5,6*]

[1]State Key Laboratory for Chemo/Biosensing and Chemometrics, College of Chemistry and Chemical Engineering, Hunan University, Changsha, Hunan 410082, [2]School of Chemistry and Chemical Engineering, Central South University of Forestry and Technology, Changsha, Hunan 410004, [3]University College London, London WC1H 0AJ, [4]University de Montreal, Montreal, Quebec H3T 1J4, [5]Department of Engineering, University of Cambridge, Cambridge CB3 0FA, [6]Department of Chemistry, University of Oxford, Oxford OX1 3QZ, [7]Department of Biochemistry, University of Oxford, Oxford OX1 3QU, [8]College of Science, China Agricultural University, Beijing 100083, [9]School of Intelligence Science and Technology, Peking University, Beijing 100871, [10]University of Toronto, Toronto, ON M5S 1A1, [11]Department of Environmental Science and Engineering, School of Energy and Power Engineering, Xi'an Jiaotong University, Xi'an 710049, [12]School of Materials Science and Engineering, Shanghai Jiao Tong University, Shanghai 20024, [13]Dyson School of Design Engineering, Imperial College London, London SW7 2BX, [14]State Key Laboratory of Structural Chemistry, Fujian Institute of Research on the Structure of Matter, Chinese Academy of Sciences (CAS), Fuzhou, Fujian 350002

**Corresponding authors: hzhchem@mit.edu; luobc21@cau.edu.cn; zhongyhuang@hnu.edu.cn; g.he@ucl.ac.uk; i.p.parkin@ucl.ac.uk; huanxin.li@ucl.ac.uk; †C. Xu, K. Li, and S. Liu contributed equally to this work.*

Cite this: *CCS Chem*. **2025**, Just Published. DOI: 10.31635/ccschem.025.202505577

Nonprecious-metal catalysts possess great potential to replace noble metals in catalysis; however, selecting efficient candidates through experiments is time-consuming and costly. Herein, we employed a data-driven virtual screening (VS) method to discover new electrocatalysts. Specifically, we identified Cu-N_2 sites for Zn-air batteries (ZABs) in harsh electrolytes by combining VS and machine learning (ML) techniques. A thermodynamically stable and highly active Cu-N_2 Lewis acid site was pinpointed using molecular dynamics (MD) simulations and density functional theory (DFT) calculations: MD simulations filtered stable structures, while DFT calculations excluded those with high overpotentials by evaluating adsorption energies of oxygen intermediates using the "Volcano plots" theory. The ML model, trained in atomic types and geometries, predicted catalysts with DFT-level accuracy. The as-predicted Cu-N_2 Lewis acid site was experimentally synthesized in a hollow nitrogen-doped octahedron carbon framework (Cu-N_2@HNOC), with a high Cu loading of 13.1 wt %. A ZAB with Cu-N_2@HNOC as the cathode catalyst showed prolonged cycling stability and a high maximum power density of 78.1 mW/cm^2. Our strategy is applicable in the quest of valuable catalysts across a wide range of applications. With the accumulation and experimental validation of datasets to improve quality, this approach is expected to accurately predict promising electrocatalysts by integrating deep ML.

Citation: *CCS Chem*. **2025**, Just Published. DOI: 10.31635/ccschem.025.202505577
Link to VoR: https://doi.org/10.31635/ccschem.025.202505577

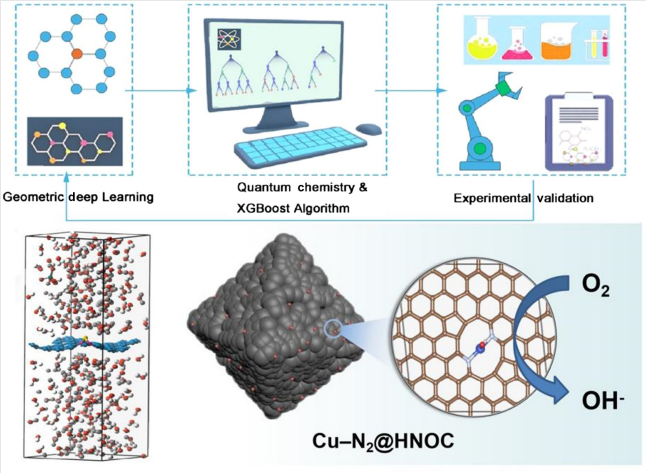

Keywords: **computer virtual screening, molecular dynamics simulation, density functional theory calculation, Cu-N_2-C, Zn-air batteries**

Introduction

The hysteresis of oxygen reduction reaction (ORR) kinetics restricts the overall development of advanced electrochemical conversion and storage devices such as metal-air batteries and fuel cells.[1–4] It is highly desirable but challenging to accelerate the reaction rate of the ORR process by introducing suitable catalysts.[5–7] Currently, Pt and its alloys are recognized as state-of-the-art ORR catalysts due to their high activity; however, these kinds of catalysts always suffer from poor methanol tolerance, high cost, and chemical susceptibility. Therefore, the exploration of nonprecious metal-based ORR catalysts with low cost, high activity, and good durability is highly desired.[8–10]

Nonprecious metal-based metal-nitrogen-carbon (M-N-C) catalysts, where a transition metal (M = Fe, Co, Ni, Cu, etc.) is incorporated into a nitrogen-doped carbon matrix (N-C), are emerging electrocatalysts.[11–13] Among them, Cu-based catalysts are regarded as promising alternatives to replace Pt owing to their acceptable price, potential ORR activity, and superior electrical conductivity.[14] Despite the intrinsic activity of Cu being lower than most nonprecious metals (including Ca, Mg, Al, Zn, Fe, Co, Ni, Sn, Pb, etc.), Cu-N_x sites were demonstrated to deliver efficient activity towards oxygen catalytic process because the N ligands significantly modulate the electronic structure of Cu, thus optimizing adsorption energies towards oxygen intermediates.[15–17] Yang et al.[18] found that Cu-N_x structures could adjust the density of states (DOS) of carbon near the Fermi level, and lower the local work function, thus promoting activity towards ORR. For Fe-N-C sites with strong O* adsorption, the intermediates' adsorption energy was reduced by increasing the coordination number to promote the activity, as proved by Lai et al.[19] Their results revealed that the oversaturated Fe-N_5 active sites showed better activity than Fe-N_4. Density functional theory (DFT) calculations attested that unsaturated Cu-N_x-C sites (e.g., Cu-N_2, Cu-N_3 sites) possessed more suitable binding energy toward oxygen intermediates than the saturated Cu-N_4-C site, thereby delivering higher ORR activity.[20–22]

However, several challenges hindered the exploration of Cu-N_x-C sites with efficient electrochemical activities. First, the search for thermodynamically stable Cu-N_x-C sites based on experimental results is an extremely time-consuming and capital-sensitive task. Furthermore, the fabrication of thermodynamically stable and highly active Cu-N_x-C sites is still challenging, especially at a high loading of single Cu atoms (>10.0 wt %). Therefore, it is not feasible to screen such catalysts based on an "inch-by-inch" search mode via typical experimental synthesis, characterization, and electrochemical measurement. Computer virtual screening (VS) technology is an efficient approach to accelerate the conventional high throughput screening (HTS) processes that have been successfully applied for new drug discovery in the pharmaceutical industry recently. The computer VS approach is expected to be applicable to search for suitable catalysts in broad areas, although no standard protocol has been established yet and to our knowledge, no case has been reported up to date.

Herein, considering the above challenges, we first used the computer VS mode to discover new efficient electrochemical catalysts, which were more cost-effective than experimental ones: We employed molecular dynamics (MD) simulation to discover coordination unsaturated Cu-N_2 Lewis acid sites that are thermodynamically stable

Citation: *CCS Chem.* **2025**, Just Published. DOI: 10.31635/ccschem.025.202505577
Link to VoR: https://doi.org/10.31635/ccschem.025.202505577

(for easy synthesis purpose) and harsh electrolytes (1 M KOH and 0.5 M H_2SO_4, for wide pH applications). Then DFT calculations were adopted to filter out those sites with high overpotential by evaluating the adsorption energies for oxygen-related adsorption intermediates based on the "Volcano plots" theory and effective description factor. The as-predicted thermodynamic stable yet the coordination-unsaturated Cu-N_2 sites were further synthesized via a facile in-situ self-template induced strategy in a hollow nitrogen-doped octahedron carbon (Cu-N_2@HNOC), in which Cu atoms were coordinated with two N atoms (Cu-N_2) in linear mode on the planar defects, confirmed by quantitative X-ray absorption spectroscopy (XAS) analysis, Raman fitting, X-ray photoelectron spectroscopy (XPS), and theoretical simulations. The synthesis of Cu-N_2@HNOC with a valence state of Cu close to +1 within a linear type of Cu-N_2 site was quite challenging, but we successfully achieved this using a straightforward in-situ self-template strategy, as outlined in the Supporting Information, built upon our previous experiments. As a result, both experimental data and DFT calculations verified that the Cu-N_2 Lewis acid sites exhibited both promising electrochemical activity (E_{onset} = 0.93 V, $E_{1/2}$ = 0.83 V, and J_L = 5.81 mA/cm^2) and long-term stability for ORR over a wide pH range. The as-prepared Cu-N_2@HNOC was also fabricated as cathode catalysts in Zn-air batteries (ZABs), delivering a peak power density of 190 mW/cm^2 at a current density of 312 mA/cm^2. Notably, the Cu-N_2-C site also exhibited the highest stability compared with the other representative nonprecious metals (Fe, Co, Ni, etc.) due to the low intrinsic activity of Cu element, and thus, a stable cycling at the acid electrolyte was achieved, outperforming the state-of-the-art ZABs.

Experimental Methods

Chemicals and materials

Copper nitrate trihydrate, zinc acetate, sodium hydroxide (NaOH), polypyrrole hydrazine hydrate (85%), hydrochloric acid (HCl, 36.0%–38.0%), potassium hydroxide (KOH), and ethanol were analytical reagent (AR) grade and purchased from Sinopharm Chemical Reagent Co. Ltd. (Shanghai, China). Zinc foil (99.9% trace metals basis), polyvinyl alcohol, commercial Pt/C (20 wt %), and RuO_2 catalysts were supplied by Sigma-Aldrich (Shanghai, China). All chemicals were used without further purification.

Synthesis of CuO octahedron

Precisely, 0.6 g of copper (II) nitrate trihydrate was dissolved in 1 L of deionized water under continuous stirring for 30 min. Subsequently, 10 mL of 2 M NaOH aqueous solution and 2 mL of 35% hydrazine hydrate were sequentially added under stirring conditions for 2 h. After centrifugation and drying at 60 °C overnight, the obtained powder was calcinated in the air at 400 °C for 30 min with a heating rate of 2 °C/min to acquire the black product, denoted as CuO octahedron.

Syntheses of Cu-N_2@HNOC

First, 0.1 g of CuO octahedron and 1 mL of pyrrole were uniformly dispersed in 50 mL of ethanol by ultrasonication for half an hour. Then 10 mL of 1 M HCl aqueous solution was added dropwise into the above suspension and kept stirred continuously for 3 h. After centrifugation and washing with deionized water and ethanol, the black product, a Cu-containing hollow polypyrrole octahedron (namely, Cu-PPY-HO) was obtained. Finally, the attained Cu-PPY-HO was pyrolyzed at 800 °C for 2 h in a N_2 atmosphere with a heating rate of 5 °C/min to obtain Cu-N_2@HNOC. For comparison, the Cu-containing HNOC was also prepared by washing Cu-PPY-HO in 1 M HCl aqueous solution and deionized water several times, followed by the same pyrolysis procedure as Cu-N_2@HNOC.

Results and Discussion

Technically, we proposed an advanced multimodal model to demonstrate the effectiveness of VS for electrocatalysts. This model integrates geometric deep learning, quantum chemistry, and the XGBoost (eXtreme Gradient Boosting) machine learning (ML) algorithm for predicting the ORR overpotential profile. The predictions were then validated experimentally. Geometric deep learning was employed to identify element types and atomic positions within chemical structures (Scheme 1a). Quantum chemistry provided fundamental physical and chemical properties regarding the ORR, as well as the electrocatalytic performance indicators for these structures (Supporting Information Figure S1), while XGBoost guided subsequent alterations to the chemical structure (Scheme 1b). The optimized chemical structure was synthesized and tested for experimental validation, with relevant data weighting adjusted based on reliability feedback from experimental outcomes (Scheme 1c). Specifically, our observations indicated that VS effectively retrieved catalyst-activity-stability relations and accurately predicted electrocatalyst structures to achieve desired properties. These functionalities hold promise for accelerating various catalyst discovery processes. Furthermore, the outcomes of such catalyst structures consistently aligned with feedback from chemical synthesis experiments, showcasing the model's adeptness in domain knowledge exploration. Scheme 1d shows the standard protocol for searching efficient M-N_x-C (M = Fe, Co, Ni, and Cu; x = 2, 3, 4, and 5) active sites. The input dataset was randomly generated by slightly modifying the graphene structural model (replacing carbon atoms

Citation: *CCS Chem.* **2025**, Just Published. DOI: 10.31635/ccschem.025.202505577
Link to VoR: https://doi.org/10.31635/ccschem.025.202505577

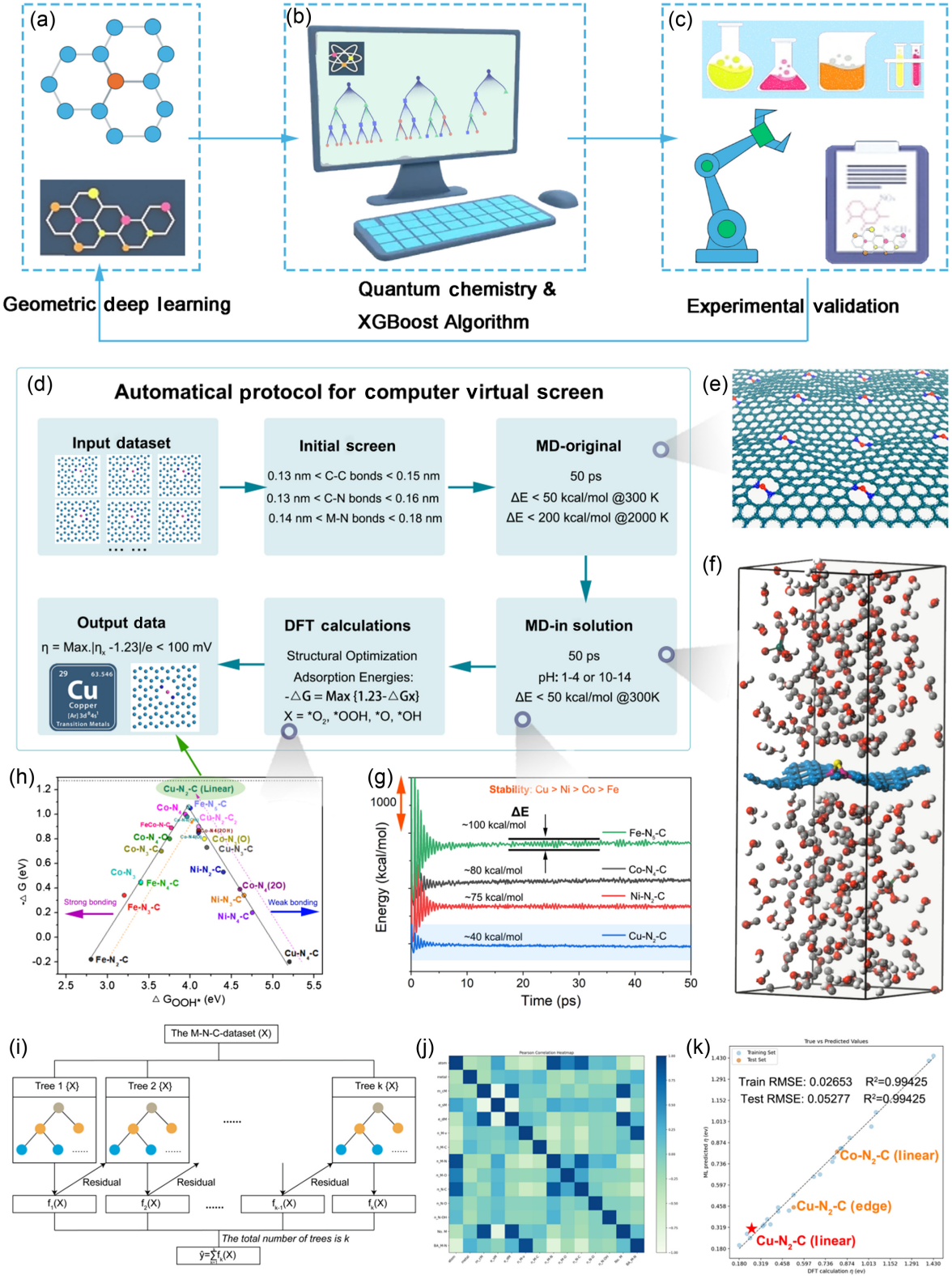

Scheme 1 | *Schematic representation of the processes for computer virtual screen: (a) geometric deep learning, (b) gaussian processes and Bayesian optimization, (c) experimental validation, (d) the standard protocol, (e) MD-screened thermodynamic stable structure from 300 to 2000 K, and (f) stability in harsh electrolyte (pH: 1–4 or 10–14), (g) energy profiles during MD and (h) band structures and adsorption energies of intermediates from DFT calculations, (i) XGBoost algorithm for ML, (j) Pearson correlation coefficient heatmap among 14 descriptors, (k) Comparison of DFT-calculated overpotential profiles with ML-predicted ones.*

Citation: *CCS Chem.* **2025**, Just Published. DOI: 10.31635/ccschem.025.202505577
Link to VoR: https://doi.org/10.31635/ccschem.025.202505577

with defects, N atoms, or Cu atoms, details in Supporting Information). Then an initial screening was conducted to check whether the bond lengths of C–C, C–N, and M–N were within a rational range. The next step was to run an MD simulation to confirm the stability of input rational structures at both room temperature and high temperature, with restrictive conditions on energy fluctuations setting as ΔE < 0.5 kcal/mol @300 K; and ΔE < 5.0 kcal/mol @2000 K within 50 ps to ensure good thermal stability, essential for easy and scalable synthesis. The representative structural model is shown in Scheme 1e. Meanwhile, the structural dynamic stability was also verified in harsh electrolyte conditions with ΔE < 0.5 kcal/mol @300 K to check the long-term durability in extremely strong acidic or alkaline electrolytes, which was the normal condition in electrocatalytic systems. Scheme 1f displays the selected structural model in an extremely acidic solution (0.5 M H_2SO_4), and Scheme 1g illustrates the energy profiles after 50 ps, indicating good stability. Moreover, the dynamic stable structures were carried out with DFT calculations to quantify the theoretical overpotential by evaluating their adsorption energies for oxygen-related adsorption intermediates, for example, *O_2, *OOH, *O, and *OH (Scheme 1h), and the potential candidate was selected based on the "Volcano plots" theory. Normally, the changes in Gibbs free energy for adsorbed oxygen-related intermediate ($\triangle G_{*OOH}$) increase with the coordination number of N (M-N_5-C > M-N_4-C > M-N_3-C > M-N_2-C), indicating the adsorption ability was altered from strong to weak. The Fe-N_x-C sites had a relatively strong adsorption ability toward intermediates, and the catalytic activity could be improved by increasing the coordination number of N. Thus, the Fe-N_5-C was on the top of the "Volcano plots," suggesting the highest catalytic activity. The opposite trend was apparent for Ni-N-C catalysts, which displayed a catalytic activity order of Ni-N_4-C > Ni-N_3-C > Ni-N_2-C due to the weak adsorption on the Ni sites. Following this rule, the catalytic activity of Cu-N_2-C sites should exceed the Cu-N_4-C and Cu-N_3-C sites, and we predict its location at the top of the "Volcano plots" according to the Gibbs free energy for *OOH. Finally, the stability of representative high-active structure models Fe-N_5-C, Co-N_4-C, Ni-N_2-C, and Cu-N_2-C were conducted with MD simulations in acid solution, resulting in energy vibrations of ~100, 80, 75, and 40 kcal/mol, which indicated that the Cu-N_2-C was the most stable structure due to the intrinsic inertness of Cu among all the high-active structure models. Only the structures with the limited energy vibration (<50 kcal/mol) for MD simulation were collected in the output data. As a result, the Cu-N_2 Lewis acid site in linear mode was predicted as a model with thermodynamic stability and high catalytic activity simultaneously.

With the accumulation of overpotential profiles from DFT calculations, it became feasible to use ML algorithms to predict catalysts based on the M-N-C dataset, which significantly accelerated the screening and prediction process. The M-N-C dataset were trained and evaluated with XGBoost (Scheme 1i), an algorithm designed to construct decision trees (DTs). XGBoost classified the M-N-C dataset by continuously building DTs and learning from misclassifications or residues. Eventually, all the DTs were combined to assist with predictions. DTs were similar to human thinking in their intelligible nature, making XGBoost an extremely competitive ML model.[23] Firstly, we collected and listed 25 selected M-N-C models as datasets (Supporting Information Figure S1). We adopted XGBoost, a ML algorithm that combined the prediction results of multiple tree models to achieve better generalization performance, for predicting the overpotential voltage for ORR. We took 14 descriptors, which could be obtained directly from the M-N-C model dataset: CN atom (coordination number of center metal), metal (type of center metal), m_cM (mass of center metal), e_*s*M (Number of electrons in the *s* orbital for center metal), e_*d*M (Number of electrons in the *d* orbital for center metal), n_M-v (number of vacant coordination for center metal), n_M-C (number of carbon coordination for the center metal), n_M-N (number of nitrogen coordination for the center metal), n_M-O (number of oxygen coordination for the center metal), n_N-C (number of nitrogen-carbon bonds), n_N-O (number of nitrogen-oxygen bonds), n_N-OH (number of N-OH bonds), No. M (Metal atomic number), and BA_M-N (bond angle of Metal-Nitrogen). We calculated the Pearson correlation among these 14 descriptors, with the heatmap shown in Scheme 1j. These 14 descriptors were then fed into the XGBoost model to predict the overpotential profile. The training objective was to minimize the root mean squared error (RMSE) between the ground-truth overpotential profile and the predicted overpotential profile. We employed grid search to select the optimal hyperparameters, including learning rate, maximum tree depth, feature subsample ratio, and the number of trees. The optimal hyperparameters are listed in the Supporting Information, and the prediction results are illustrated in Scheme 1k. The training RMSE was 0.02653 and the test RMSE was 0.05277, indicating that the predicted data aligned well with the DFT data. The Cu-N_2-C (linear) model was identified as the predicted electrocatalytic site for ORR with low overpotential (denoted by the red star in Scheme 1k). We further demonstrated feature importance in Supporting Information Figure S2, where the CN atom played the most significant role (17.8%), followed by metal (15.8%), m_cM (11.6%), n_M-N (11.0%), n_M-C (8.9%), and BA_M-N (7.5%). The other features were less important, each with less than 7% abundance. In summary, this ML algorithm enabled accurate evaluation and prediction of electrocatalyst performance based on the atomic types and geometric model of M-N-C profiles. Additionally, it provided insights into the design

Citation: *CCS Chem.* **2025**, Just Published. DOI: 10.31635/ccschem.025.202505577
Link to VoR: https://doi.org/10.31635/ccschem.025.202505577

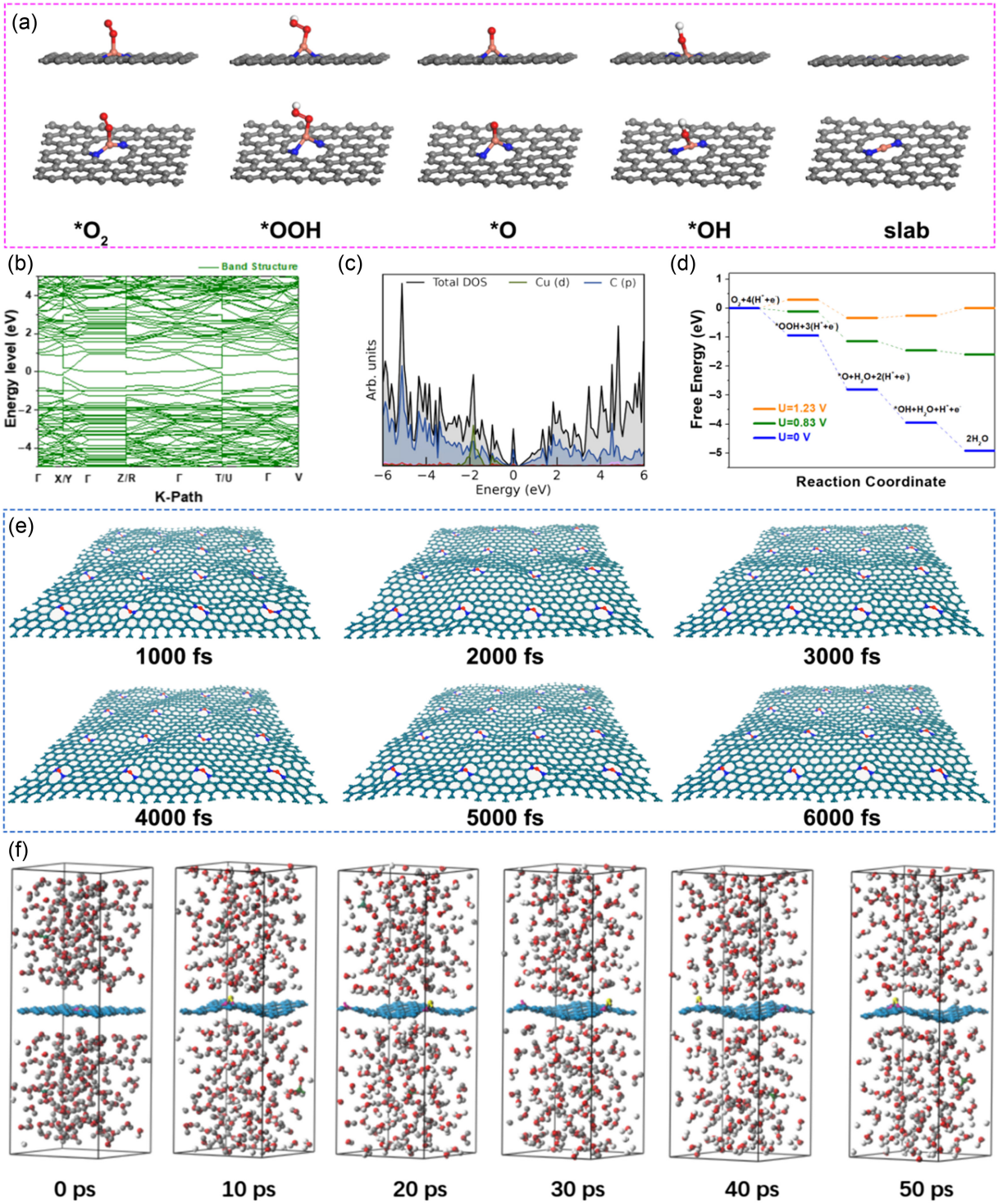

Figure 1 | *(a) Top (up) and side (down) views of the optimized configuration of oxygen intermediate species adsorbed on the Cu-N_2-C; (b) The band structure for Cu-N_2-C; (c) ORR free energy diagrams at different potentials for Cu-N_2-C; (d) Gibbs free energy changes for oxygen-containing intermediates on Cu-N_2-C; (e) the MD simulation at 2000 K and (f) in 0.5 M H_2SO_4 solution for Cu-N_2-C model.*

principles and basis of optimization for M-N-C by highlighting the importance of various features.

To demonstrate the catalytic activity and thermodynamic stability of the Cu-N_2 Lewis acid site in linear mode for ORR, detailed MD and DFT simulations in the VS protocol were illustrated. The model of Cu-N_2-C sites was built up by replacing two carbon atoms in opposite positions with nitrogen atoms and removing adjacent carbon

Citation: *CCS Chem.* **2025**, Just Published. DOI: 10.31635/ccschem.025.202505577
Link to VoR: https://doi.org/10.31635/ccschem.025.202505577

atoms to create defects for the two coordinated copper atoms. The adsorption behavior for $*O_2$, *OOH, *O, and *OH intermediates on Cu-N_2-C sites is illustrated in Figure 1a, suggesting that the Cu center is the active site for ORR. The band structure of the as-constructed Cu-N_2-C is shown in Figure 1b, indicating an enrichment of DOS near the Fermi level compared with ideal graphene (zero at the Fermi level). The increase in DOS observed in Cu-N_2-C compared with ideal graphene directly correlated with an enhanced ability to adsorb and activate oxygen intermediates, thereby improving its catalytic efficiency. The electronic structure tuning via Cu–N coordination represents a promising strategy for designing advanced carbon-based catalysts. The model for Cu-N_2-C exhibited moderate free energies for intermediate adsorption and removal, making the energy barriers more average for all steps. The band structure for Cu-N_2-C (Figure 1c) demonstrated a relatively high density of states as the electron cloud appears near the Fermi level, indicating an enhanced conductivity compared with conventional graphitized carbon materials. The free energies of intermediates on the Cu-N_2-C model for ORR processes at different voltages are shown in Figure 1d (seeSupporting Information Tables S6–S8 for more details), indicating that the step from $*O_2$ to *OOH was the rate-determining step (RDS) at 1.23 V. The energy barriers for each step revealed a low overpotential of 0.29 V for the whole ORR process. Therefore, the low energy barrier was achieved for Cu-N_2-C due to the modulated band structures and DOS, which promoted the kinetics for ORR catalytic processes. Moreover, thermodynamic stability was as important as catalytic activity for practical applications. Thus, the MD simulation (Figure 1e) was carried out to investigate the possible degradation of Cu-N_2-C under a high temperature (2000 K). The simulation results showed that the Cu-N_2-C skeleton structure became wavy but remained undamaged, and all Cu single atoms were well-fixed by N atoms without any aggregation. The MD simulation suggested that the as-prepared Cu-N_2@HNOC catalyst possessed a coordination, unsaturated but thermodynamically stable structure, endowing possibly good cyclability of the catalyst. The corresponding high-resolution transmission electron microscopy (HR-TEM) mapping images (Supporting Information Figures S3 and S4) and XPS spectra (Supporting Information Figure S5) of Cu-N_2@HNOC catalyst after 2000 K heat-treatment indicated the Cu single atom persisted (the boiling point of copper was above 2900 K) and the Cu–N bonds and structures remained unchanged, which verified the good stability of the Cu-N_2 Lewis acid structure under high temperature. In addition, the Cu-N_2-C in 0.5 M H_2SO_4 solution was also simulated by MD (Figure 1f, Supporting Information Figure S6, and Videos S1–S6) to understand the possible degradation behaviors of Cu-N_2@HNOC in aqueous acidic electrolytes. The results revealed that (1) the Cu-N_2-C skeleton structure became wavy and the molecule (H_2O) and ions (H_3O^+, OH^-) in aqueous electrolytes tended to approach the surface of Cu-N_2-C layer, indicating the good hydrophilicity and wettability; (2) the aqueous acidic electrolyte did not etch the Cu-N_2-C skeleton structure due to the strong coordination bond between the Cu and N atoms, ensuring the excellent catalytic activity and stability of the unsaturated Cu-N_2 Lewis acid sites. It is worth mentioning that the cost of discovering a new catalyst via VS was much lower than that through experimental approaches. We estimated and compared the cost, time, and energy consumption for evaluating the activity and stability of an individual catalyst via experimental or computer VS approach, and suggested that the VS would be a more cost-, time-, and energy-efficient way of reducing the cost, time, and energy consumption by 80%, 90% and 60%, respectively (Supporting Information Figure S7 and Tables S1–S3).

To further verify the accuracy of the algorithm and VS protocol, the as-predicted Cu-N_2 Lewis acid site was experimentally synthesized in a hollow nitrogen-doped octahedron carbon framework (Cu-N_2@HNOC), in which an ultrahigh loading of single Cu atoms (13.1 wt % by inductively coupled plasma mass spectrometry (ICP-MS) was achieved. As presented in Figure 2a, Cu-N_2@HNOC was fabricated by in-situ polymerization followed by pyrolysis. First, a CuO octahedron with an average diameter of 500 nm (Figure 2b) was prepared by a simple chemical reduction method. The X-ray diffraction (XRD) pattern (Supporting Information Figure S8a) and Raman spectrum (Supporting Information Figure S8b) were indexed to the typical characteristic peaks of CuO. Then the CuO template was mixed with pyrrole monomers under ultrasonication. Subsequently, with the addition of diluted HCl solution, Cu^{2+} ions were gradually released, which initiated the polymerization of pyrrole under the surface of the octahedron template until CuO was entirely dissolved. Meanwhile, Cu^{2+} ions used as the oxidant were reduced to low valence states and trapped by the nitrogen-containing groups of the polymers. The obtained Cu-containing hollow polypyrrole octahedron (Cu-ppy-HO) exhibited the original octahedron shapes (Figure 2c), but the diameter was slightly larger than that of the pristine CuO octahedron due to the successful deposition of polypyrrole. The XRD result (Supporting Information Figure S8a) also demonstrated the existence of polypyrrole and the disappearance of CuO after in-situ polymerization. Finally, the Cu-ppy-HO was annealed in a N_2 atmosphere to obtain the final product of Cu-N_2@HNOC. As depicted in Figure 2d, Cu-N_2@HNOC presented identical octahedron structures with rough surfaces and hollow structures (in the red circle). The TEM image (Figure 2e) also verified its hollow octahedron structure with inner and outer diameters of 500 and 700 nm, respectively, suggesting the thickness of the carbon shell layer was around 100 nm. The HR-TEM image (Figure 2f) showed a typical amorphous carbon

Citation: *CCS Chem.* **2025**, Just Published. DOI: 10.31635/ccschem.025.202505577
Link to VoR: https://doi.org/10.31635/ccschem.025.202505577

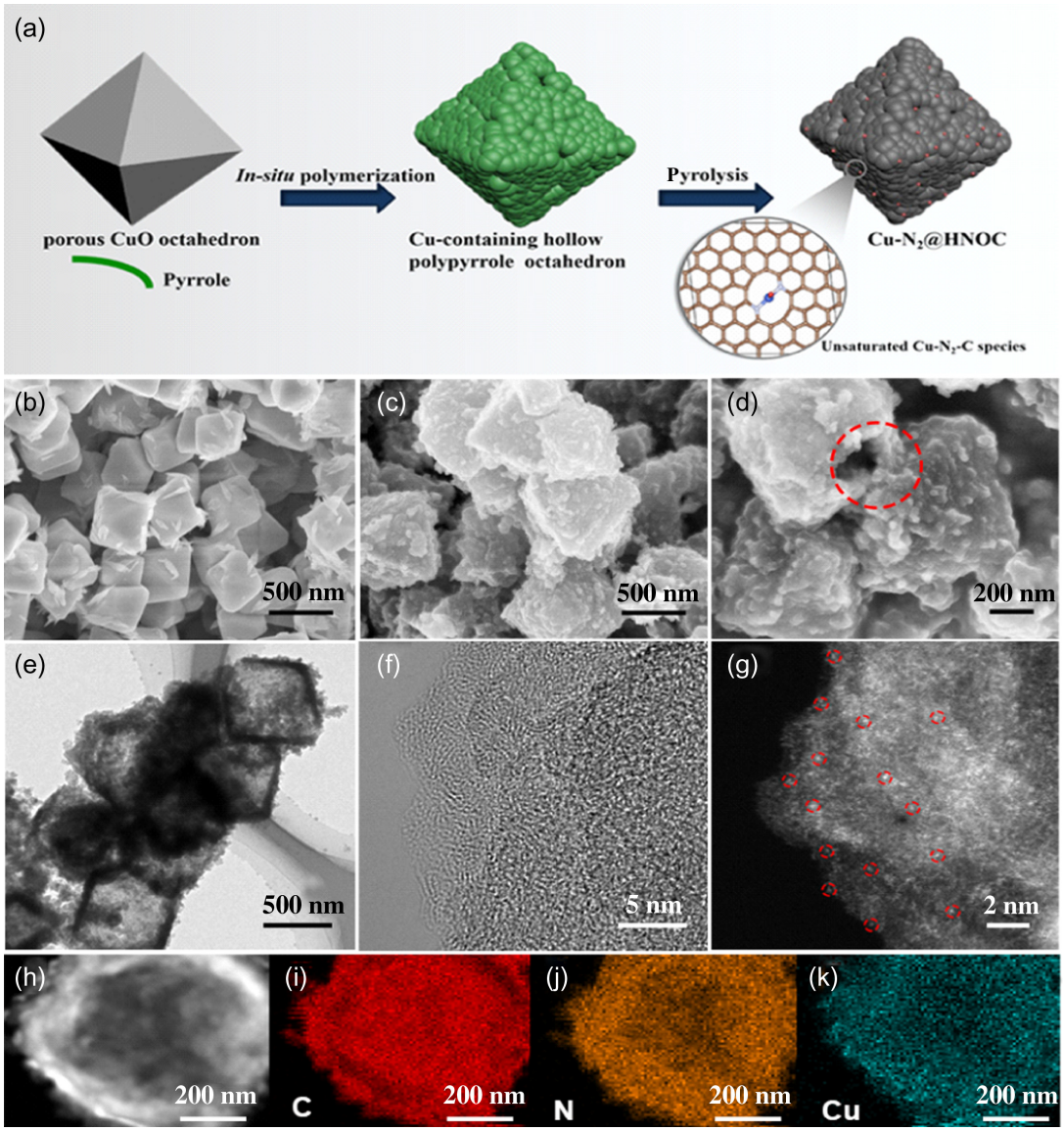

Figure 2 | *(a) Schematic representation of the fabrication process of Cu-N_2@HNOC; SEM images of (b) CuO, (c) Cu-ppy HCO, (d) Cu-N_2@HNOC; (e) TEM image, (f) HR-TEM image, (g) aberration-corrected HAADF-STEM images, and (h–k) corresponding EDS mapping images of Cu-N_2@HNOC.*

structure without any metal fingerprint, which corresponded to the XRD results (Supporting Information Figure S8a) indicating that there were no peaks of metallic Cu or other compounds in Cu-N_2@HNOC. Furthermore, only some concentrated bright particles could be observed in the aberration-corrected high-angle annular dark-field scanning transmission electron microscopy (AC HADDF-STEM) image (Figure 2g), suggesting the existence of atomic-scale Cu sites. The abundant and uniformly dispersed Cu atoms, identified by the isolated bright dots, could have acted as efficient active sites for superior catalytic ability. Moreover, the typical energy dispersive X-ray spectroscopy (EDS) mapping images of Cu-N_2@HNOC (Figure 2h) disclosed that high-loading nitrogen and copper atoms were distributed evenly on the carbon matrix by this in-situ polymerization strategy. ICP-MS confirmed that the Cu content of 13.1 wt % in Cu-N_2@HNOC was consistent with the result of thermo gravimetric analysis (Supporting Information Figure S9).

XPS measurements were carried out to explore the state of each chemical composition. A survey spectrum (Supporting Information Figure S10) showed that Cu–N_2@HNOC contained C, N, O, and Cu elements. In the N *1s* fine spectrum (Supporting Information Figure S11a and Table S4), the peaks were assigned to pyridinic-N, Cu-N, pyrrolic-N, and graphitic-N. The peak at 399.1 eV matched the Cu–N structure and its content exceeded a quarter, suggesting the abundant Cu–N bonds in

Citation: *CCS Chem.* **2025**, Just Published. DOI: 10.31635/ccschem.025.202505577
Link to VoR: https://doi.org/10.31635/ccschem.025.202505577

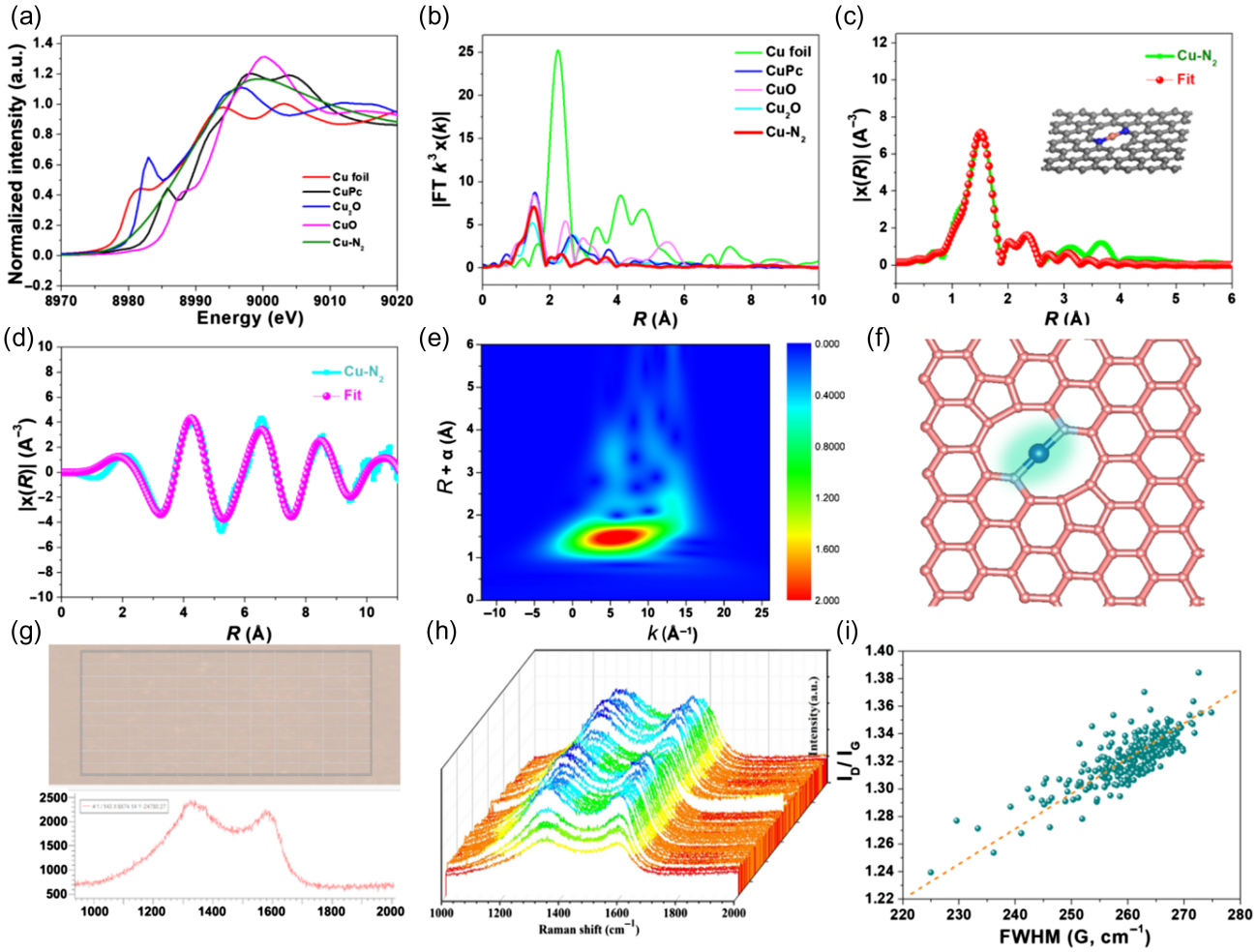

Figure 3 | *Cu k-edge XANES spectra (a) and Fourier-transformed EXAFS (b) of Cu-N_2@HNOC, Cu foil, CuPc, Cu_2O and CuO; The Cu EXAFS fitting curve in* R *space (c) and in* k *space (d) of Cu* k*-edge with Cu-N_2 model; (e) The corresponding WT plots; (f) Schematic model of Cu-N_2 structure; (g) Raman mapping image and typical Raman spectrum; (h) 143 single-point spectra in Raman mapping area; (i) The plots of I_D/I_G as a function of FWHM for the 143 single-point Raman spectra in Cu-N_2@HNOC.*

Cu-N_2@HNOC.[22] The high-resolution Cu 2p spectrum (Supporting Information Figure S11b) deconvoluted into two peaks at 931.6 and 951.6 eV, assigned to Cu(I) $2p_{1/2}$ and Cu(I) $2p_{3/2}$ respectively.[22] The results were consistent with previous reports, which revealed that the valence of Cu in the unsaturated Cu-N_x-C sites approached +1, while the valence of Cu in saturated Cu-N_4-C was close to +2.[24,25] The coordination environment and chemical state of Cu atoms were further analyzed by XAS analysis. Figure 3a shows the normalized X-ray absorption near edge structure (XANES) curve of the Cu *k*-edge. The absorption edge of Cu–N_2@HNOC was located between the Cu foil and Cu phthalocyanine (CuPc), suggesting that the oxidation state of Cu species in Cu–N_2@HNOC was between 0 and 2 (higher than Cu^0 and lower than Cu^{2+}). The *k*-space extended X-ray adsorption fine structure (EXAFS) spectra of Cu foil, CuO, Cu_2O, CuPc, and Cu–N_2@HNOC are illustrated in Supporting Information Figure S12. The coordination environment of Cu was fitted by the k^3-weighted Fourier transforms (FT) of EXAFS (Figure 3b). The result for Cu–N_2@HNOC showed the existence of a main peak at 1.5 Å, attributed to the Cu–N scattering path, according to the referred characteristic peak of the Cu–N bond in CuPc. The metallic Cu–Cu peaks at ~2.2 Å in Cu–N_2@HNOC were negligible, indicating the Cu atoms were isolated from each other. The FT-EXAFS fitting results quantified the atomic-coordination numbers of the central Cu atom with N atoms in the first coordination shell, where the k^3-weighted FT-EXAFS curves were well-fitted with the linear Cu-N_2 model in both *R* space (Figure 3c) and *k* space (Figure 3d). The detailed fitting for Cu–N_2@HNOC with angled Cu-N_2-C, linear Cu-N_2-C, Cu-N_3-C, and Cu-N_4-C models is shown in Supporting Information Figure S13, indicating the linear Cu-N_2 model was the best-matched structural fitting.

Citation: *CCS Chem.* **2025**, Just Published. DOI: 10.31635/ccschem.025.202505577
Link to VoR: https://doi.org/10.31635/ccschem.025.202505577

Furthermore, the wavelet transform (WT) plot is depicted in Figure 3e and Supporting Information Figure S14. The intensity maximum of Cu foil was centered around 8 Å, corresponding to the Cu–Cu bonding. In contrast, the maximum of Cu-N_2@HNOC appeared at 4–6 Å, close to that of CoPc, assigned to the contribution of Cu–N bonding. More detailed structural parameters are listed in Supporting Information Table S5. The coordination number of Cu-N_2@HNOC was 2.11 ± 0.24, as confirmed by XAS. Compared with Cu-N_4 sites, unsaturated Cu-N_2sites (Figure 3f) were more favorable for O_2 adsorption and O–O bond stretching; thus, Cu-N_2@HNOC was expected to deliver an impressive ORR performance. Raman spectroscopy was used to identify the structure of the Cu-N_2 sites in Cu-N_2@HNOC. Figure 3g shows the Raman selected area mapping and a typical spectrum for Cu-N_2@HNOC, which demonstrated the characteristic D peak (~1350 cm^{-1}) and G peak (~1580 cm^{-1}) for graphite carbon.[26] Figure 3h illustrates the 143 single-point Raman spectra within the mapping area, where the Raman signals showed slight shifts and changes in position and changes in full width at half maximum (FWHM). The plots of I_D/I_G as a function of FWHM for the 143 single-point spectra in Raman mapping were fitted (Figure 3i), indicating the existence of basal plane defects rather than edge defects in the Cu-N_2@HNOC since the I_D/I_G is correlated with the FWHM (G),[27] consistent with the XAS fitting.

In addition, the porosity and specific surface area were investigated by the N_2 adsorption/desorption isotherm (Supporting Information Figure S15a). The curve for Cu-N_2@HNOC displayed Type IV isotherms, indicating abundant mesopores. The pore size distribution curves (inset) revealed mainly pore sizes under 10 nm, referring to abundant micro/mesopores located on the octahedron surface. The hollow and hierarchical porous structure provided the prerequisite for a highly efficient ORR process due to accelerated electron/mass transport and more exposed active sites.[28–30] To further explore the effect of Cu-N_2 sites, we prepared HNOC control samples for comparison. The XRD and Raman techniques for HNOC and Cu-N_2@HNOC were performed to get an insight into the crystal structures and defects. As shown in Supporting Information Figure S15b, all the XRD curves displayed a broadened peak located at ~26°, assigned to carbon. In comparison, the peaks for Cu-N_2@HNOC shifted negatively compared with those of HNOC, which might be due to the incorporation of Cu atoms, resulting in a larger lattice spacing. The Raman spectra in Supporting Information Figure S15c present the value of I_D/I_G. Specifically, the values of Cu-N_2@HNOC (1.32) were much larger than that of HNOC (1.07), indicating that the introduction of Cu atoms led to higher defect densities, thus providing more active sites for ORR.[3,31]

The electrochemical catalytic activity toward ORR was investigated by the rotating disk electrode (RDE) technique in 0.1 M KOH solution. Figure 4a depicts the cyclic voltammetry (CV) of different electrodes. Obviously, all the CV curves exhibited quasi-rectangular capacitive background current in the N_2–saturated solution but possessed a strong oxygen reduction peak in an O_2–saturated solution. Moreover, the peak for Cu-N_2@HNOC (0.84 V), located at the most positive position, was much more positive than that for HNOC (0.70 V). This signified that the Cu-N_2@HNOC electrode possessed better catalytic activity toward ORR. This supposition was also supported by the linear sweep voltammetry (LSV) results. As shown in Figure 4b, the Cu-N_2@HNOC electrode presented prominent activity with more positive onset potential (E_{onset}, 0.93 V) and half-wave potential ($E_{1/2}$, 0.83 V), with a higher limiting current density (J_L) of 5.81 mA/cm^2 compared with the Pt/C electrode (E_{onset} = 0.92 V, $E_{1/2}$ = 0.81 V, J_L = 5.48 mA/cm^2). Moreover, the LSV curves at different rotation rates and the corresponding Koutecky-Levich (K–L) plots at different potentials of Cu-N_2@HNOC are given in Figure 4c. The electron transfer number (n) at the potential range from 0.2 to 0.4 V indicated a one-step reaction mechanism, followed by the direct four-electron transfer pathway. To discern the reaction kinetics, the kinetic current density (J_k) at a potential of 0.75 V and a Tafel plot was obtained, as shown in Figure 4d,e. Compared with other counterparts, the Cu-N_2@HNOC electrode exhibited higher values of J_k (23.6 mA/cm^2) and smaller Tafel slopes (80 mV/dec), suggesting its faster reaction kinetics and better ORR activity. The superior electrochemical performance of Cu-N_2@HNOC was associated with the synergistic effect of highly active unsaturated Cu-N_2 sites and hollow porous structures. The resultant electronic structure furnished prominent activity. It is well-known that the metal-N structure is sensitive to the thiocyanate ion (SCN^-), thus, we employed the SCN^- solution to detect the Cu-N_x active site. As shown in Supporting Information Figure S16, the ORR activity of Cu-N_2@HNOC exhibited a significant drop after adding 0.01 M SCN^-, illustrating the blockage of the Cu-N_2 site. Whereas, the HNOC catalyst displayed no significant variation because the SCN^- could not poison the nitrogen catalytic sites.[13] In addition, the durability test was conducted by chronoamperometric tests. As revealed in Figure 4f, the current recession of Cu-N_2@HNOC was only 6.5% after 20,000 s, but the loss of Pt/C was 18.3%. The scanning electron microscopy (SEM) image of Cu-N_2@HNOC after ORR cycling is presented in Supporting Information Figure S17. As shown, Cu-N_2@HNOC retained its original octahedral morphology without any collapse. Undoubtedly, Cu-N_2@HNOC displayed considerable stability, ascribed to the intrinsic thermodynamic structural stability of Cu-N_2 Lewis acid sites, as well as the hollow octahedron structure with abundant hierarchical pores, avoiding the possible collapse during the mass and electron transport.[13,14] Furthermore, a methanol tolerance test was conducted

Citation: *CCS Chem.* **2025**, Just Published. DOI: 10.31635/ccschem.025.202505577
Link to VoR: https://doi.org/10.31635/ccschem.025.202505577

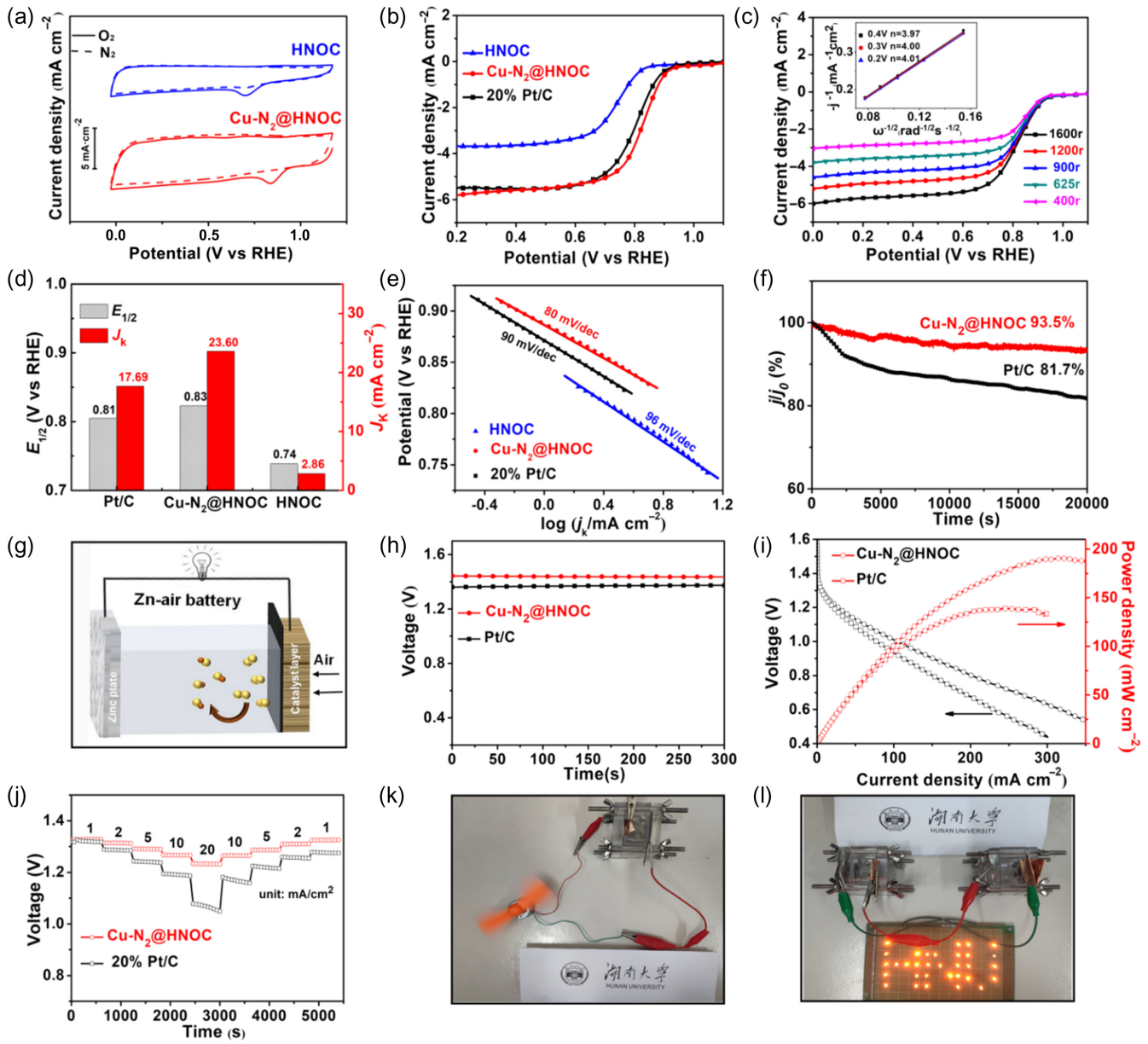

Figure 4 | *(a) CV curves in N_2/O_2 saturated 0.1 M KOH electrolyte and (b) LSV curves at the rotation rate of 1600 rpm of various electrocatalysts; (c) LSV curves of Cu-N_2@HNOC electrode at different rotation rates from 400 to 1600 rpm and the corresponding K–L plots (inset); Comparison of $E_{1/2}$ and J_k values (d) and Tafel slopes (e) on different electrocatalysts; (f) Chronoamperometric curves on Cu-N_2@HNOC and 20% Pt/C catalysts; (g) Schematic illustration of aqueous ZABs assembled with Cu-N_2@HNOC as cathode catalysts; (h) Open circuit voltage measurements (i) Discharge polarization curves and the power density curve; (j) Discharge curves at various current densities; (k) Photograph of a fan powered by one ZAB; (l) Photograph of some red LED bulbs powered by two ZABs connected in series.*

(Supporting Information Figure S18) in which a sharp current loss occurred at Pt/C after the introduction of 3 M methanol. In contrast, negligible degradation was observed for Cu-N_2@HNOC, suggesting superior anti-methanol poison ability.

To assess the potential for practical application, the obtained Cu-N_2@HNOC was applied as the cathode catalyst in homemade ZABs; (Figure 4g). The ZABs assembled with Cu-N_2@HNOC displayed an open-circuit voltage of 1.44 V, higher than that of Pt/C (1.37 V; Figure 4h). As shown in Figure 4i, the ZABs based on Cu-N_2@HNOC delivered a peak power density of 190 mW/cm^2 at a current density of 312 mA/cm^2, superior to that of Pt/C (139 mW/cm^2 at 241 mA/cm^2) under the same conditions. The Cu-N_2@HNOC catalyst also exhibited good rate performance, as revealed in Figure 4j,

Citation: *CCS Chem.* **2025**, Just Published. DOI: 10.31635/ccschem.025.202505577
Link to VoR: https://doi.org/10.31635/ccschem.025.202505577

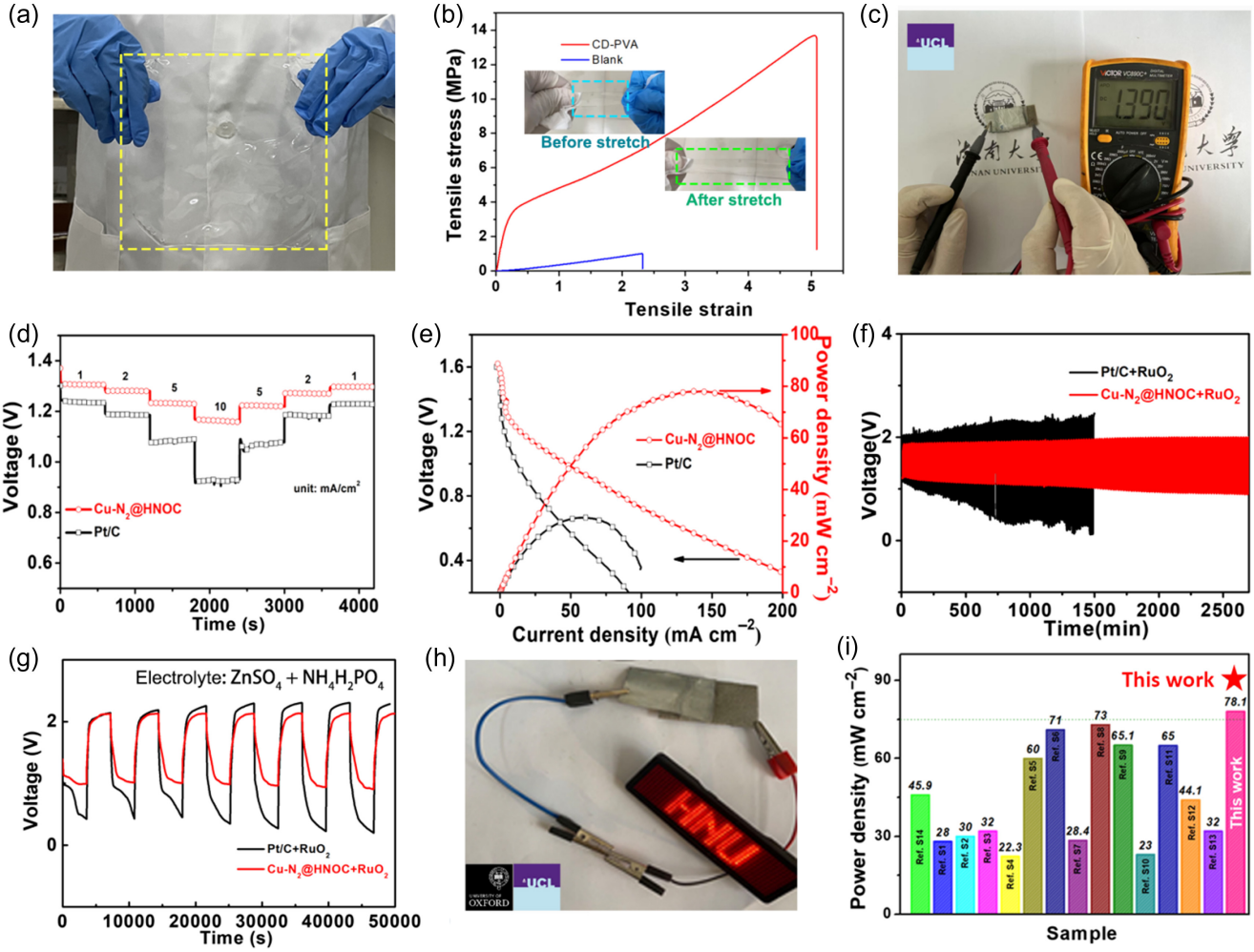

Figure 5 | *(a) Optical image of CD-PVA film; (b) the tensile stress of CD-PVA and normal PVA, inset: the optical images before and after stretch; (c) the diagram of flexible solid-state ZABs and the open voltage; (d) Rate performance, (e) Polarization and power density and (f) Galvanostatic charge-discharge at 3 mA cm^{-2} for solid-state ZABs with different electrocatalysts; (g) The charging-discharging curve of solid-state ZABs in acid electrolyte (1 M $ZnSO_4$+ $NH_4H_2PO_4$, pH = 4–5); (h) Photographs of LED light charged by solid-state ZABs; (i) The comparison of the Cu-N_2@HNOC ZAB with representative work reported previously.*

since there was only a small voltage drop when the current density increased to 20 mA/cm^2, with a voltage recovery to the initial value once the current density returned to 1 mA/cm^2. Therefore, ZABs based on Cu-N_2@HNOC catalyst could drive a small fan benefiting from the high power density (Figure 4k), and two ZABs could be integrated in series to power light emitting diode (LED 3 V) bulbs (Figure 4l). Additionally, primary ZABs with the Cu-N_2@HNOC catalyst had favorable durability and rate performance. Normalized to the mass of consumed Zn, the specific capacity of Cu-N_2@HNOC was calculated to be 700.82 mAh/kg_{Zn} (Supporting Information Figure S19a). The galvanostatic discharge curves at 5 mA/cm^2 (Supporting Information Figure S19b) displayed a stable discharge potential of 1.27 V, and only a slight decline of output voltage was observed within nearly 45 h, demonstrating excellent stability. Furthermore, rechargeable ZABs were also constructed with a mixture of RuO_2 and Cu-N_2@HNOC catalysts. It was discerned that only a very small voltage change happened after 200 cycles (Supporting Information Figure S20), suggesting excellent rechargeability and application potential.[32]

To further prove the practical applications of Cu-N_2@HNOC for the ZAB devices, flexible solid-state ZABs were also fabricated. The stability and flexibility of solid-state ZABs were promoted by casting-drying polyvinyl alcohol (CD-PVA) gel electrolyte (10 ×10 cm^2 CD-PVA film in Figure 5a). The optimized CD-PVA film possessed a maximum tensile stress of 13.5 MPa, ten times higher than the normal PVA film (Figure 5b). Moreover, the ion mobility of the CD-PVA film was higher than the normal

Citation: *CCS Chem.* **2025**, Just Published. DOI: 10.31635/ccschem.025.202505577
Link to VoR: https://doi.org/10.31635/ccschem.025.202505577

one (Supporting Information Figure S21). Ni foam and CD-PVA film were used as a current collector and solid-state electrolyte. The optimized ZAB delivered a high open-circuit voltage of 1.39 V (Figure 5c). Notably, only a small voltage drop was observed in Figure 5d for Cu-N_2@HNOC when the current density increased from 1 to 10 mA cm^{-2}, suggesting its excellent rate performance.[33,34] As shown in Figure 5e, Cu-N_2@HNOC catalyst displayed a peak power density of 78.1 mW cm^{-2}, much higher than that of Pt/C under the same conditions. Performance tests on flexible solid-state ZABs with various bending angles were also conducted. As shown in the Supporting Information Figure S22, ZAB delivered high open circuit voltages of 1.360, 1.387, 1.336, and 1.349 V when bent at 0°, 45°, 90°, and 120°, respectively. Furthermore, when the Cu-N_2@HNOC-based flexible ZAB was folded in different bending states, only a negligible increase in voltage gap was observed in Supporting Information Figure S23, demonstrating its exceptional mechanical robustness and operational stability.[35] In addition, Cu-N_2@HNOC catalyst-based ZAB presented favorable durability with no obvious voltage change after cycling for a long time, suggesting a promising application prospect (Figure 5f). Besides, ZAB with the Cu-N_2@HNOC catalyst operated well under acid electrolyte (pH = 4–5), with a voltage of 1.0–1.1 V for discharging and 2.0–2.1 V for charging (Figure 5g, the first report for SSZABs under acidic conditions). Furthermore, the solid-state ZABs with only ~3 cm^2 achieved a high power density ascribed to the high catalytic activity of Cu-N_2@HNOC, which was able to light up LED series displaying the letters "HNU" (abbreviation of Hunan University) (Figure 5h**)**. In a word, the ZAB with Cu-N_2@HNOC cathode is still competitive with the up-to-date state-of-the-art ZABs (Figure 5i and Supporting Information Table S9).

Limitations and Perspective

One limitation of this work is the insufficiency of high-quality data. While numerous structures are available from both theoretical and experimental perspectives, the lack of a standardized protocol renders the results incomparable, and datasets in existing studies might yield misleading outcomes. Addressing this limitation could significantly improve the research, but it might necessitate support from the entire scientific community in the future. Another bottleneck is the expressiveness of chemical structure models. Enhancing the development of more expressive architectures could be feasibly integrated into the multimodal pretraining framework. For future directions, we aim to establish a universal platform and a standardized protocol for retrieving catalyst-activity-stability relations via VS. These results would be continuously updated following experimental validation. With the accumulation of high-quality input datasets, accurately predicting electrocatalyst structures to achieve desired properties could be achieved more effectively.

Conclusion

In summary, a computer VS standard protocol was developed and built up by combining MD simulations, DFT calculations, and ML. A thermodynamically stable yet coordination-unsaturated Cu-N_2 Lewis acid site was discovered to possess promising electrochemical activity via this protocol. The as-screened Cu-N_2 Lewis acid site was fabricated in a Cu-N_2@HNOC through a facile in-situ polymerization, followed by a pyrolysis strategy using CuO octahedrons as self-sacrificial templates. The obtained Cu-N_2@HNOC exhibited excellent performance in ORR and ZABs, attributed to the synergistic effect of hollow nitrogen-doped carbon structures and highly active unsaturated Cu-N_2 sites. Specifically, the unsaturated coordination of Cu-N_2 Lewis acid sites modulated the charge distribution, adsorption energy, and hydrophilicity, and thus, improved the catalytic activity, as predicted by the DFT calculations, MD simulations, and validation through the experimental results. The thermodynamics and catalytic operating stability of the unsaturated linear Cu-N_2 site were verified by MD simulation. The thermodynamically stable yet coordination-unsaturated Cu-N_2 Lewis acid sites provided new insights and good guidance for the search and design of high-performance Cu-based electrocatalysts. Although the current protocol was used to screen the Cu-N-C-based catalysts, it could be used for the discovery of multiple types of functional materials.

Supporting Information

Supporting Information is available and includes supplementary notes, figures (S1–S23), and tables (S1–S9).

Author Contributions

Huanxin Li conceived and designed the study idea; he cowrote the paper, supervised the entire project, and was responsible for the infrastructure and project direction. Chenxi Xu, Kaiqi Li, Shengchao Liu, and Huanxin Li discussed the idea, wrote the code, experimentally realized the study, analyzed the data and cowrote the paper. These works were assisted by Junwei Xu, Subash Sharma, Jincan Zhang, Boyang Mao, Haotian Chen, Hao Zhang, Hannan Xu, Bingcheng Luo, Haiteng Zhao, Zhuoxinran Li, Zhongyuan Huang, Jianan Wang, Kai Xi, Chaopeng Fu, Yunlong Zhao, Guoliang Chai, Guanjie He, and Ivan Parkin. All the authors discussed the results, commented on, and revised the manuscript.

Citation: *CCS Chem.* **2025**, Just Published. DOI: 10.31635/ccschem.025.202505577
Link to VoR: https://doi.org/10.31635/ccschem.025.202505577

Conflict of Interest

The authors declare no conflict of interest

Acknowledgments

This work was supported by National Natural Science Foundation of China (grant nos. 52274298, 51974114, 51672075, and 2190804), International Postdoctoral Exchange Fellowship Program, China (grant no. PC2022020), the Natural Science Foundation of Hunan Province, China (grant nos. 2024JJ4022 and 2025JJ60382), the Scientific Research Fund of Hunan Provincial Education Department, China (grant no. 24B0270), Technology Innovation Program of Hunan Province, China (grant no. 2020RC2024), and China Postdoctoral Science Foundation (grant nos. 2020M682560 and GZC20233205). The National Supercomputing Center in Changsha, China, is acknowledged for allowing the use of computational resources. K.L. would like to thank the China Scholarship Council/UCL Dean's Prize for the joint PhD funding. Engineering and Physical Sciences Research Council (EPSRC), United Kingdom, is thanked for funding through EP/L015862/1. Richard G. Compton from the University of Oxford, United Kingdom, assisted with the proofreading of the manuscript.

Preprint Acknowledgment

The research presented in this article was posted on a preprint server prior to publication in CCS Chemistry. The corresponding preprint article can be found here: 10.21203/rs.3.rs-3635532/v1.

References

1. Gallagher, J. Oxygen Reduction Reaction: Counting Active Sites. *Nat. Energy* **2016**, *1*, 16198.
2. Zhou, Y.; Yu, Y.; Ma, D.; Foucher, A. C.; Xiong, L.; Zhang, J.; Stach, E. A.; Yue, Q.; Kang, Y. Atomic Fe Dispersed Hierarchical Mesoporous Fe–N–C Nanostructures for an Efficient Oxygen Reduction Reaction. *ACS Catal.* **2021**, *11*, 74–81.
3. Sun, Z.; Wang, Y.; Zhang, L.; Wu, H.; Jin, Y.; Li, Y.; Shi, Y.; Zhu, T.; Mao, H.; Liu, J.; Xiao, C.; Ding, S. Simultaneously Realizing Rapid Electron Transfer and Mass Transport in Jellyfish-Like Mott–Schottky Nanoreactors for Oxygen Reduction Reaction. *Adv. Funct. Mater.* **2020**, *30*, 1910482.
4. Chen, H.; Liang, X.; Liu, Y.; Ai, X.; Asefa, T.; Zou, X. Active Site Engineering in Porous Electrocatalysts. *Adv. Mater.* **2020**, *32*, 2002435.
5. Li, H.; Gong, Y.; Zhou, H.; Li, J.; Yang, K.; Mao, B.; Zhang, J.; Shi, Y.; Deng, J.; Mao, M.; Huang, Z.; Jiao, S.; Kuang, Y.; Zhao, Y.; Luo, S. Ampere-Hour-Scale Soft-Package Potassium–Ion Hybrid Capacitors Enabling 6-Minute Fast-Charging. *Nat. Commun.* **2023**, *14*, 6407.
6. Yang, X.; Zheng, X.; Li, H.; Luo, B.; He, Y.; Yao, Y.; Zhou, H.; Yan, Z.; Kuang, Y.; Huang, Z. Non-Noble-Metal Catalyst and Zn/Graphene Film for Low-Cost and Ultra-Long-Durability Solid-State Zn–Air Batteries in Harsh Electrolytes. *Adv. Funct. Mater.* **2022**, *32*, 2200397.
7. Shen, H.; Gracia-Espino, E.; Ma, J.; Zang, K.; Luo, J.; Wang, L.; Gao, S.; Mamat, X.; Hu, G.; Wagberg, T.; Guo, S. Synergistic Effects Between Atomically Dispersed Fe–N–C and C–S–C for the Oxygen Reduction Reaction in Acidic Media. *Angew. Chem. Int. Ed.* **2017**, *56*, 13800–13804.
8. Cheng, R.; He, X.; Li, K.; Ran, B.; Zhang, X.; Qin, Y.; He, G.; Li, H.; Fu, C. Rational Design of Organic Electrocatalysts for Hydrogen and Oxygen Electrocatalytic Applications. *Adv. Mater.* **2024**, *36*, 2402184.
9. Wu, J.; Zhou, H.; Li, Q.; Chen, M.; Wan, J.; Zhang, N.; Xiong, L.; Li, S.; Xia, B. Y.; Feng, G.; Liu, M.; Huang, L. Densely Populated Isolated Single Co-N Site for Efficient Oxygen Electrocatalysis. *Adv. Energy Mater.* **2019**, *9*, 1900149.
10. Xu, C.; Wu, J.; Chen, L.; Gong, Y.; Mao, B.; Zhang, J.; Deng, J.; Mao, M.; Shi, Y.; Hou, Z.; Cao, M.; Li, H.; Zhou, H.; Huang, Z.; Kuang, Y. Boric Acid–Assisted Pyrolysis for High-Loading Single-Atom Catalysts to Boost Oxygen Reduction Reaction in Zn–Air Batteries. *Energy Environ. Mater.* **2024**, *7*, e12569.
11. Zhao, L.; Zhang, Y.; Huang, L. B.; Liu, X. Z.; Zhang, Q. H.; He, C.; Wu, Z. Y.; Zhang, L. J.; Wu, J.; Yang, W.; Gu, L.; Hu, J. S.; Wan, L. J. Cascade Anchoring Strategy for General Mass Production of High-Loading Single-Atomic Metal-Nitrogen Catalysts. *Nat. Commun.* **2019**, *10*, 1278.
12. Li, J.; Chen, J.; Wang, H.; Ren, Y.; Liu, K.; Tang, Y.; Shao, M. Fe/N Co-Doped Carbon Materials with Controllable Structure as Highly Efficient Electrocatalysts for Oxygen Reduction Reaction in Al-Air Batteries. *Energy Storage Mater.* **2017**, *8*, 49–58.
13. Huang, Z.; Pan, H.; Yang, W.; Zhou, H.; Gao, N.; Fu, C.; Li, S.; Li, H.; Kuang, Y. In Situ Self-Template Synthesis of Fe-N-Doped Double-Shelled Hollow Carbon Microspheres for Oxygen Reduction Reaction. *ACS Nano* **2018**, *12*, 208–216.
14. Tan, Z.; Li, H.; Feng, Q.; Jiang, L.; Pan, H.; Huang, Z.; Zhou, Q.; Zhou, H.; Ma, S.; Kuang, Y. One-Pot Synthesis of Fe/N/S-Doped Porous Carbon Nanotubes for Efficient Oxygen Reduction Reaction. *J. Mater. Chem. A* **2019**, *7*, 1607–1615.
15. Lai, Q.; Zhu, J.; Zhao, Y.; Liang, Y.; He, J.; Chen, J. MOF-Based Metal-Doping-Induced Synthesis of Hierarchical Porous Cu-N/C Oxygen Reduction Electrocatalysts for Zn–Air Batteries. *Small* **2017**, *13*, 1700740.
16. Zhang, Y.; Liu, J.; Wang, J.; Zhao, Y.; Luo, D.; Yu, A.; Wang, X.; Chen, Z. Engineering Oversaturated Fe-N_5 Multifunctional Catalytic Sites for Durable Lithium-Sulfur Batteries. *Angew. Chem. Int. Ed.* **2021**, *60*, 26622–26629.
17. Li, P.; Jin, Z.; Qian, Y.; Fang, Z.; Xiao, D.; Yu, G. Supramolecular Confinement of Single Cu Atoms in Hydrogel Frameworks for Oxygen Reduction Electrocatalysis with High Atom Utilization. *Mater. Today* **2020**, *35*, 78–86.
18. Yang, Z.; Chen, B.; Chen, W.; Qu, Y.; Zhou, F.; Zhao, C.; Xu, Q.; Zhang, Q.; Duan, X.; Wu, Y. Direct Transformation of

Copper(I) Oxide Bulk into Isolated Single-Atom Copper Sites Catalyst Through Gas-Transport Approach. *Nat. Commun.* **2019**, *10*, 3734.
19. Lai, Q.; Zheng, L.; Liang, Y.; He, J.; Zhao, J.; Chen, J. Metal–Organic-Framework-Derived Fe-N/C Electrocatalyst with Five-Coordinated Fe-N_x Sites for Advanced Oxygen Reduction in Acid Media. *ACS Catal.* **2017**, *7*, 1655–1663.
20. Li, F.; Han, G.-F.; Noh, H.-J.; Kim, S.-J.; Lu, Y.; Jeong, H. Y.; Fu, Z.; Baek, J.-B. Boosting Oxygen Reduction Catalysis with Abundant Copper Single-Atom Active Sites. *Energy Environ. Sci.* **2018**, *11*, 2263–2269.
21. Wu, H.; Li, H.; Zhao, X.; Liu, Q.; Wang, J.; Xiao, J.; Xie, S.; Si, R.; Yang, F.; Miao, S.; Guo, X.; Wang, G.; Bao, X. Highly Doped and Exposed Cu(I)–N Active Sites within Graphene Towards Efficient Oxygen Reduction for Zinc–Air Batteries. *Energy Environ. Sci.* **2016**, *9*, 3736–3745.
22. Yang, J.; Liu, W.; Xu, M.; Liu, X.; Qi, H.; Zhang, L.; Yang, X.; Niu, S.; Zhou, D.; Liu, Y.; Su, Y.; Li, J.; Tian, Z. Q.; Zhou, W.; Wang, A.; Zhang, T. Dynamic Behavior of Single-Atom Catalysts in Electrocatalysis: Identification of Cu-N_3 as an Active Site for the Oxygen Reduction Reaction. *J. Am. Chem. Soc.* **2021**, *143*, 14530–14539.
23. Mládek A.; Gerla V.; Zazay A.; Bradáč, O. Application of Machine Learning Methods in NPH. In *Normal Pressure Hydrocephalus: Pathophysiology, Diagnosis, Treatment and Outcome*;Bradac, O., Ed.; Springer International Publishing: Cham, **2023**; pp 359–386.
24. Li, J.; Xia, W.; Wang, T.; Zheng, L.; Lai, Y.; Pan, J.; Jiang, C.; Song, L.; Wang, M.; Zhang, H.; Chen, N.; Chen, G.; He, J. A Facile Route for Constructing Effective Cu-N_x Active Sites for Oxygen Reduction Reaction. *Chem. Eur. J.* **2020**, *26*, 4070–4079.
25. Jiang, Z.; Sun, W.; Shang, H.; Chen, W.; Sun, T.; Li, H.; Dong, J.; Zhou, J.; Li, Z.; Wang, Y.; Cao, R.; Sarangi, R.; Yang, Z.; Wang, D.; Zhang, J.; Li, Y. Atomic Interface Effect of a Single Atom Copper Catalyst for Enhanced Oxygen Reduction Reactions. *Energy Environ. Sci.* **2019**, *12*, 3508–3514
26. Liu, X.; Liu, Y.; Jin, M.; Xu, C.; Tian, Y.; Zhou, M.; Wang, W.; Li, G.; Hou, Z.; Chen, L. Construction of N-Doped Carbon Encapsulated Mn_2O_3/MnO Heterojunction for Enhanced Lithium Storage Performance. *J. Colloid Interface Sci.* **2024**, *665*, 752–763.
27. Ferrari, A. C.; Basko, D. M. Raman Spectroscopy as a Versatile Tool for Studying the Properties of Graphene. *Nat. Nanotechnol.* **2013**, *8*, 235–246.
28. Liu, Y. P.; Xu, C. X.; Ren, W.Q.; Hu, L. Y.; Fu, W. B.; Wang, W.; Yin, H.; He, B. H.; Hou, Z. H.; Chen, L. Self-Template Synthesis of Peapod-Like MnO@N-Doped Hollow Carbon Nanotubes as an Advanced Anode for Lithium-Ion Batteries. *Rare Met.* **2023**, *42*, 929–939.
29. Zhou, L.; Zhuang, Z.; Zhao, H.; Lin, M.; Zhao, D.; Mai, L. Intricate Hollow Structures: Controlled Synthesis and Applications in Energy Storage and Conversion. *Adv. Mater.* **2017**, *29*, 1602914.
30. Zhu, W.; Chen, Z.; Pan, Y.; Dai, R.; Wu, Y.; Zhuang, Z.; Wang, D.; Peng, Q.; Chen, C.; Li, Y. Functionalization of Hollow Nanomaterials for Catalytic Applications: Nanoreactor Construction. *Adv. Mater.* **2019**, *31*, 1800426.
31. Hou, J.; Sun, Y.; Wu, Y.; Cao, S.; Sun, L. Promoting Active Sites in Core–Shell Nanowire Array as Mott–Schottky Electrocatalysts for Efficient and Stable Overall Water Splitting. *Adv. Funct. Mater.* **2018**, *28*, 1704447.
32. Li, H.; Wen, Y.; Jiang, M.; Yao, Y.; Zhou, H.; Huang, Z.; Li, J.; Jiao, S.; Kuang, Y.; Luo, S. Understanding of Neighboring Fe-N_4-C and Co-N_4-C Dual Active Centers for Oxygen Reduction Reaction. *Adv. Funct. Mater.* **2021**, *31*, 2011289.
33. Li, S.; Chen, W.; Pan, H.; Cao, Y.; Jiang, Z.; Tian, X.; Hao, X.; Maiyalagan, T.; Jiang, Z. FeCo Alloy Nanoparticles Coated by an Ultrathin N-Doped Carbon Layer and Encapsulated in Carbon Nanotubes as a Highly Efficient Bifunctional Air Electrode for Rechargeable Zn-Air Batteries. *ACS Sustainable Chem. Eng.* **2019**, *7*, 8530–8541.
34. Rao, P.; Yu, Y.; Wang, S.; Zhou, Y.; Wu, X.; Li, K.; Qi, A.; Deng, P.; Cheng, Y.; Li, J.; Miao, Z.; Tian X. Understanding the Improvement Mechanism of Plasma Etching Treatment on Oxygen Reduction Reaction Catalysts. *Exploration* **2023**, *4*, 20230034.
35. Hao, X.; Jiang, Z.; Zhang, B.; Tian, X.; Song, C.; Wang, L.; Maiyalagan, T.; Hao, X.; Jiang, Z. N-Doped Carbon Nanotubes Derived from Graphene Oxide with Embedment of FeCo Nanoparticles as Bifunctional Air Electrode for Rechargeable Liquid and Flexible All-Solid-State Zinc-Air Batteries. *Adv. Sci.* **2021**, *8*, 2004572.

Citation: *CCS Chem.* **2025**, Just Published. DOI: 10.31635/ccschem.025.202505577
Link to VoR: https://doi.org/10.31635/ccschem.025.202505577